Master's Thesis

Saturation Intensity of Rare Earth Ions Doped Crystals

A step towards quantum computing

Author:
Martynas Solovejus

Supervisor:
PhD Student Jenny Karlsson
Assistant Supervisor:
Professor Stefan Kröll

Lund University

Faculty of Science
Division of Atomic Physics
Quantum Information Group

VT 2014

Abstract

The thesis is primarily concerned with rare earth ions doped into yttrium ortho silicate crystals, RE:YSO. It is considered to be an ambitious platform for the development of quantum computing schemes. One such scheme requires the detection of single cerium ions. The project was aimed at measuring the saturation intensity of cerium 5d-4f transition which is needed for the single ion detection.

This work contains theoretical simulations as well as measurements of fluorescence from rare earth ions sitting inside of a crystal as a function of excitation power. For practical reasons the measurement could not be carried out on cerium, but praseodymium was used instead.

By measuring the saturation intensity one can derive the homogeneous linewidth that contributes to the detection procedure. The major complication in this type of measurement is the power broadening. Therefore, the measurement was aided by a theoretical simulation.

The data was then fit with simulated theoretical results. The measurement was inconclusive for several reasons that are discussed at the end. However, this work is a priceless reference for the future cerium saturation intensity measurement or another experiment that needs to consider power broadening effects.

Acronyms

CCD Charge coupled device

RE Rare-earth

REICQ Rare-earth ions based quantum computing

RRR Residual resistivity ratio

ZPL Zero-phonon line

Contents

1 Introduction

The story of computing is a story of collective work and the convergence of many different areas, where the advance in one field is highly dependent on progress in other, sometimes strikingly remote, fields. With an increasing understanding of the quantum behaviour forefront of research have moved to the manipulations of matter on an atomic scale. Likewise, the most ambitious advance of computational technology is now in the hands of atomic physicists who have to unravel the atomic properties of a host substance in order to gain the sufficient knowledge needed for quantum control. It is of one such atomic property needed for better understanding of atomic behaviour that is the niche this thesis aiming to fill. A brief look into the background is necessary to see the motivation behind this work.

The novelty of a quantum computer is better understood by knowing the principles of an ordinary computer – its paradigmatic companion – which the former is promising to surpass. Instead of the decimal system, the digital paradigm uses a binary form, only 0 and 1's, to code information, perform and control computations. The basic unit of information that can have one of the two values is called a *bit*. The straightforward advantage of this deduction to a two-level representation was that it could be easily stored in a two-level physical device and it was soon realised that the information describing such a two-level system could be easily transported as electrical pulses. As a result the new paradigm coupled with the advance in underlying electronics technology led to steady progress in computational technology that is well illustrated by the "Moore's law". In 1965 chemist Gordon Moore made an empirical observation that the storage capacity of computer memory chips grows steadily, doubling every 18 months [1]. In recent decades the phenomena was mainly driven by the decrease in transistor size. However, as the size of transistor is heading towards atomic dimensions, the law is said to be reaching its physical limit [2]. On the atomic scale the performance is hindered by quantum effects and can no longer be controlled by classical methods of information treatment. However, the idea of 'quantum computer' introduced by Richard Feynman in 1982 suggested the asserted limit to be technological rather than physical, while rather than being an obstacle the quantum behaviour turned out to provide computational advantage allowing a coherent superposition of two states – the *qubit*.

The quantum information group in Lund University is working on a quantum computing scheme that takes advantage of the atomic structure of rare-earth (RE) ions sitting in a solid state crystal, normally referred to as *rare-earth ions based quantum computing* or REIQC scheme [3]. There are a few apparent benefits of such a configuration. First, the coherent superposition of two energy levels can be preserved over a series of computational steps. The latter is satisfied by the weakly allowed 4f-4f transition that due to the shielding provided by 5s and 5p subshells (see Figure 1) can stay in coherent superposition over a period longer than 10000 optical pulses. Second, the insertion of dopant ions into a regular crystalline structure results in lattice strains disturbing the uniform electric field. As a result of disturbances due to the local electric field each sub-ensemble of ions gains a characteristic shift of excited energy level within a corresponding inhomogeneous linewidth (see figure 4 in section 2.2). A sub-ensemble stands for a qubit that in turn can be selectively addressed via fre-

quency space by probing an inhomogeneously broadened absorption spectrum. A qubit-qubit interaction necessary for implementation of binary arithmetic is realised via permanent electric ion-ion dipole interaction between closely spaced ions in each qubit [4].

The above satisfies two fundamental conditions required for a quantum computer: the realisation of the qubit and interaction of multiple qubits. This gives sufficient motivation for the experimental work necessary testing and completing the REICQ scheme where with the aid of laser pulses these randomly distributed ions could be structured into a functional quantum computer, in addition a qubit initialisation was demonstrated by Rippe et al. [5]. However, due to random dopant ion positioning spatially dependant permanent dipole-dipole interaction complicates the task of creating a large number of interacting qubits [4]. This introduces the *scalability* problem, i.e. the ability to scale up a system to multiple qubits. A single ion approach was proposed as a solution to this problem by Wesenberg et al. [3], where instead of an ensemble a qubit is represented by a single ion. As the direct readout of a state becomes difficult, an additional cerium ion is introduced into the crystal lattice to serve as the readout ion. It is related to the neighbouring qubit ion via dipole-dipole interaction. When the qubit is in the state $|1\rangle$ the Ce ion interacts with the readout laser emitting florescence, but when the qubit is in $|0\rangle$ — permanent dipole-dipole interaction with the nearby qubit shifts the homogeneous linewidth of Ce ion out of the resonance with the laser and no fluorescence can be observed. In such a way the qubit state can be read out while the states of other qubits that are not directly coupled to the readout ion can be interpreted using conditional gate operations.

The substantial part of work carried out in the quantum information group is currently devoted to the readout scheme of the cerium ion. The master thesis undertaken is aiming to work out one of the properties necessary for completion of the scheme. This is done by a combination of computer simulation and experiment, namely, the saturation intensity measurement of the Ce^{+3} readout ion in Y_2SiO_5 crystal environment. In turn this would allow the verification or specification of the previously measured homogeneous linewidth [6] that is crucial to know for an efficient single ion qubit readout. Sadly, the Ce^{+3} excitation laser has failed during the course of the project and a substitute experiment on Pr^{+3} to confirm the validity of the simulation was conduced instead.

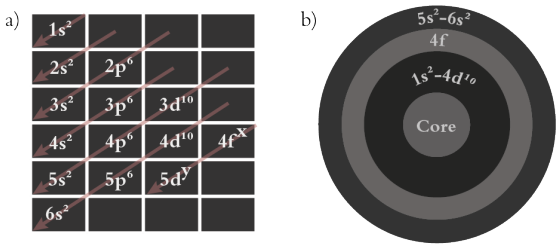

Figure 1: a) The increasing number of electrons in an atom occupy certain energy levels following the order indicated by the arrows. In case of RE ion each element has a corresponding electron number combination in their last 4f and 5d subshells, indicated as x & y respectively [7]. b) Due to the peculiar shell filling pattern part of rare-earth elements have their 4f subshell partially filled, and hence apt to manipulation yet shielded from the environment by fully filled higher order subshells.

2 Theory

The physics behind this work is primarily concerned with light interacting with rare earth (RE) ions in Y_2SiO_5 (yttrium silicate) crystal environment. It is therefore appropriate to discuss the energy structure of the relevant RE ions and look at how this structure interacts with laser light.

'1One of the reasons rare earth compounds are considered to be an attractive candidate for quantum computing applications is that they have the narrowest spectral lines among solids comparable to those of single atoms or molecules [8]. That implies that the interaction between RE ions and the environment is weak, and the narrow lines make them suitable for experiments that require a long coherence time. However, the effects of a crystalline environment not just allow sharp transitions but also result in *inhomogeneous broadening*. However, the broadening that is turned into an advantage for the quantum computing application [3] becomes an obstacle for the *saturation intensity* measurement.

We are specifically interested in Pr^{+3} 4f intra-orbital transition and the 4f-5d transition of Ce^{+3}. Under certain conditions both transitions can be approximated to behave as a two level system. Hence, two-level atom theory is employed to derive the formula for the power broadening calculation showing the intense laser light influence on the absorption properties and how the saturation effects manifest.

2.1 The energy level structure of RE ions

The saturation intensity measurement involves manipulations of RE^{+3} energy states which requires a thorough understanding of the energy level structure. The following section is thus devoted to general energy level features of the addressed RE ions as well as the concrete cases of Ce^{+3} and Pr^{+3} ions in the Y_2SiO_5 environment.

The narrow transition lines in the spectra of RE compounds originate from intra-orbital transitions within the 4f subshell. Otherwise forbidden transitions are weakly allowed due to broken symmetry in the electric field that is caused by irregularities in the crystal lattice. The narrow linewidth is made possible by the shielding provided by completely filled outer-lying 5s and 5p subshells that decouple 4f from the noise of the crystal environment (see figure 1). Contrary to 4f, the 5d subshell is not shielded by 5s, 5p and experiences much stronger exposure to the crystal field and hence the 4f-5d transition is much broader.

Ce:YSO energy levels

In case of the Ce^{+3} ion we are interested in the 4f-5d transition. The two levels of the transition experience different exposures to the external fields, hence the energy levels are shifted in different magnitudes (see figure 2 to see two different representations of the same transition). In case of the 4f level as for all RE^{+3} ions the subshell is shielded from the environment hence the level splits into the fine structure (as governed by the LS coupling [9]) while the crystal field splitting is negligible as compared to the former. In contrast, the 5d level is much more exposed to the crystal fields so the magnitude of the crystal splitting is much larger and dominant over the spin-orbit coupling. In addition, both levels

interact with the vibrational modes of the crystal, or *phonons*, that broaden the energy levels.

For cryogenic temperatures weak phonons can be approximated by the harmonic potential. Appointing such an approximation to each of the energy levels involved into transition one finds a transition between the ground states of harmonic potentials of both energy levels that is not effected by the vibrational motion of the crystal. It is referred to as the *zero phonon line*, ZPL. As it stated by Yan [4], at low temperatures ZPLs dominate the spectra of the 4f-4f transition, while the 4f-5d transition is dominated by phonon bands resulting from displacement of harmonic potentials (see figure 2). However, at cryogenic temperatures the phonon broadening influence is greatly reduced and a ZPL transition can be singled out (see figure 2b).

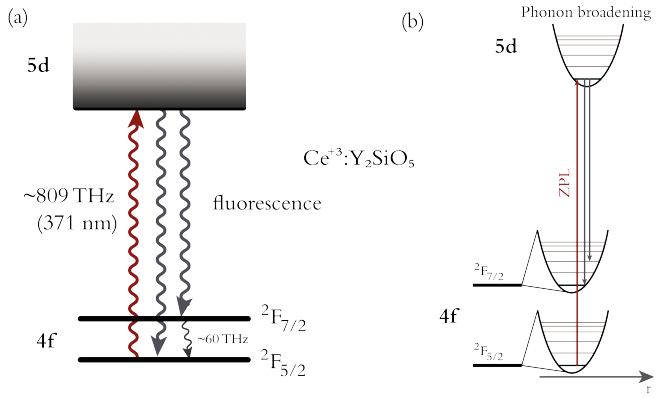

Figure 2: Ce^{+3}:Y_2SiO_5. Due to exposure to the crystal environment the structure of 5d of Ce cannot be sharply defined. At low temperatures a sharp 4f-5d transition can be singled out at 370.7 nm corresponding to the ZPL. The ideas for images are borrowed from other works [6;10].(a) The excited 5d level is represented as a band broadened due to electron –phonon coupling as compared to sharply defined fine structure of the 4f ground level (the phonon interaction is present in the ground level as well, but at cryogenic temperatures the ions would always be in the lowest (zero) phonon level). (b) The other way to represent the transition is to look at the phonon broadened levels; the ZPL stands for the energy transfer path during excitation while other arrows represent possible de-excitation paths. The potentials are designatedly displaced to show that as the overlay of electron wavefunctions is weak, hence the ZPL is not the most probable transition.

Pr:YSO energy levels

Contrary to Ce^{+3} the finest energy level splittings of Pr^{+3} are constituted by the hyperfine structure. Normally, the hyperfine splittings are determined by the electronic shell interacting with nuclear magnetic and electric moments, but in this case it is the second order hyperfine interaction that comes into play [7]. The nuclear spin couples to the crystal field splitting the lowest crystal-field state of the $^3H_4$ of the ground state into three hyperfine levels with $m_I = \pm 5/2$, $\pm 3/2$ and $\pm 1/2$. As the crystal field gives an important contribution, the splittings differ depending on which crystal hosts the Pr^{+3} ion. Since the experiments

carried out in this paper uses yttrium silicate as the host, a schematic energy level diagram of the latter is given in figure 3 below.

Under certain conditions the $^3H_4 \rightarrow {}^1D_2$ transition can be approximated to be a two-level system. At high temperatures the transitions are so broad in frequency that the nine different transitions from the hyperfine levels in the ground state to the hyperfine levels in the excited state all overlap. By exciting one transition all other transitions are excited. At low temperatures transitions become narrow and only one transitions at the time is excited. Two level approximation no longer hold as optical pumping occurs instead.

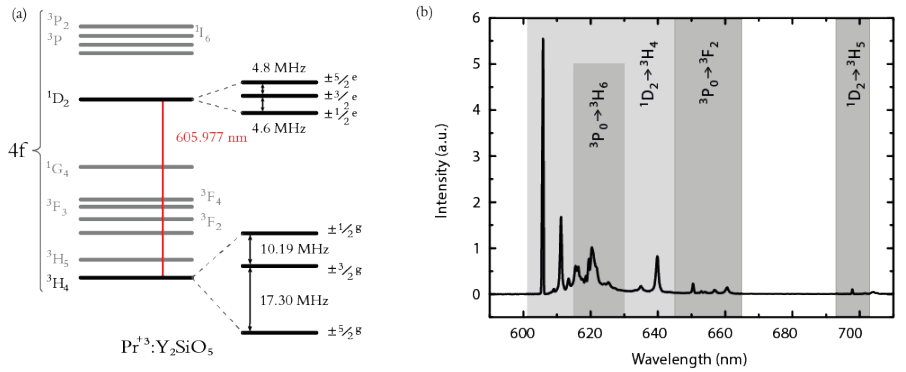

Figure 3: (a) The fine structure of 4f shell of Pr^{+3} in Y_2SiO_5. Both ground ($^3H_4$) and excited ($^1D_2$) levels split into three hyperfine doubly degenerate energy levels. The image is made with inspiration from a similar image for another transition [11]. (b) The fluorescence emission spectra of bulk Pr^{+3}:Y_2SiO_5 recorded at 4.3K temperature by Utikal et al. [11]. The spectrum was obtained by exciting $^3H_4 \rightarrow {}^3P_0$ transition using the optical repumping technique that excites all three hyperfine levels of the ground state simulataneously. The excitation laser was polarized parallel to the D_1 axis and the fluorescence measured. The spectrum of resulting fluorescence transitions is indicated in the graph. The fluorsence from higher energy level $^3P_0$ is not relevant to the work of this thesis and is ignored in the further study. The rest of the fluorescence spectrum resulting from decaying $^1D_2$ level correponds to to the spectrum that this work is aiming to detect and study.

2.2 Two broadening mechanisms

There are two distinct line broadening mechanisms that manifest in the crystalline environment with doped ions. Being intrinsic to all transitions the first mechanism is independent of the local environment and is identified as *homogeneous* broadening. As the result of crystal lattice strains these otherwise identical optical transitions with their corresponding homogeneous linewidth spread out in a Gaussian distribution [12] around the central frequency forming the second – inhomogeneous – broadening.

When an ion in a higher energy level de-excites to a lower the emitted photon has the frequency corresponding to the energy difference between the two. Accordingly, the emitted light shows as a homogeneously broadened spectral line as compared to perfectly monochromatic emission. This indeterminacy in energy difference stems from a finite coherence time. Depending on the transition in question it can be both a lot shorter than the lifetime of the excited energy level and as long as twice the lifetime, but for a specific transition in a specific ion the coherence is always the same. The homogeneous linewidth, Γ_h, is related to the coherence time, τ_2, as $\Gamma_h = 1/(\pi\tau_2)$ [12]. In contrast to the inhomogeneous case, Γ_{in}, the homogeneously broadened line is best fit by a Lorenzian profile. Similarly, the inhomogeneous broadening has a characteristic line shape function and central frequency depending on the ion in question as well as the host crystal and the doping concentration.

The presence of the inhomogeneous broadening distinguishes RE ions in a crystal from free ions and counts as an advantage when quantum computing application is considered. However, the presence of the inhomogeneous broadening introduces the effect of power broadening that complicates the measurement of saturation intensity.

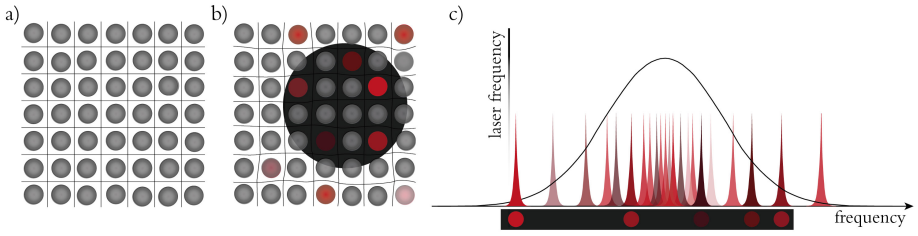

Figure 4: a) A schematic representation of the regular lattice structure of a host material (Y_2SiO_5 in our case). b) The regularity of the lattice is disturbed by dopant ions (Ce^{+3} or Pr^{+3}) resulting in field variations that in turn induce changes the energy levels of ions. There is a number of ions with varying transition frequencies within the diffraction limited laser excitation volume (marked as a black circle). c) Detuned transitions spread out over a range of values in a Gaussian distribution. Taking the advantage of the inhomogeneous broadening the number of addressed ions within the excitation volume can be further reduced by the selectivity via frequency.

2.3 Saturation Intensity

Depending on the intensity of incoming laser light a medium exposed to this light exhibits two distinct absorption patterns. For low intensities the amount of power absorbed by a medium increases linearly with incoming power. In case of high intensities linear behaviour is disrupted by the saturation effect – the net absorption of a medium decreases with increasing intensity until no net absorption is present.

In this section the theory describing the absorption properties of a two-level atom model is introduced. The effect of saturation in absorption spectroscopy is explained by looking at how intense laser light interacts with a medium hosting the population of identical two-level systems, which is later generalised to suit the RE^{+3} case.

Two-level case

A two-level system represents an idealised atom with two levels of energy, E_2 and E_1. Such a system gets excited to the upper level by absorbing a photon of the resonant radiation and de-excited to the lower level by emitting one.

When exposed to the resonant laser field with angular frequency ω=(E_2-E_1)/$\hbar$ an atom interacts with it either by photon *absorption* with the proportionality coefficient B_{12}, or by *stimulated emission*, B_{21}, and $B_{12} = \frac{g_1}{g_2}B_{21}$ [9], where g_1 and g_2 are the degeneracies of respective energy levels. The symmetry between the two is broken by *spontaneous emission* that stands for the decay from the upper to the lower level and is denoted by A_{21}. The above coefficients are determined by the intrinsic properties of the relevant atom and are referred to as *Einstein's coefficients*, see figure 5a. The explicit derivation of Einstein coefficients starting with basic atomic properties using time-dependent perturbation theory can be found in chapter 7 of Foot [9].

In the absence of radiation a medium is in thermal equilibrium, which implies that most of the population is in the lower state (*Bolzman distribution* [12]). During the exposure to radiation atoms get excited from a lower to an upper level. By increasing the intensity the proportion of excited atoms increases respectively. At some certain point the intensity is reached where half of the population is excited to the upper energy level, in consequence the absorption of the medium falls to the half of the initial. However, as the large part of the population is in the excited state, laser light forces atoms in the upper level to undergo stimulated emission which leads to the gain of emission and hence compensates for some of the absorption. As a result, there is no net absorption for high intensities.

As it is stated by Foot [9] the differential expression describing the attenuation of intense laser light in the crystal is given by:

$$\frac{dI}{dz} = -\kappa(\omega)I(\omega) = -(N_1 - N_2)\sigma(\omega)I(\omega), \tag{1}$$

while the difference in population densities can be expressed as:

$$N_1 - N_2 = \frac{N}{1 + 2I(\omega)\sigma(\omega)/(\hbar\omega A_{21})} = \frac{N}{1 + I/I_s(\omega)}. \tag{2}$$

In these equations I stands for intensity of the incoming light, N_1 and N_2 are the population densities of lower and upper energy levels and z is the depth

of the crystal, while N stands for the total number density of atoms that are interacting with light. The angular frequency dependent absorption coefficient is denoted as $\kappa(\omega)$, where the absorption cross-section of an atom characterising the probability of incident radiation absorption is denoted as $\sigma(\omega)$. The *saturation intensity* is defined from the above equations as:

$$I_s(\omega) = \frac{\hbar\omega A_{21}}{2\sigma(\omega)}. \tag{3}$$

By combining equations (1) & (2) the absorption coefficient can be expressed in terms of I and ω:

$$\kappa(\omega, I) = \frac{N\sigma(\omega)}{1 + I/I_s(\omega)}. \tag{4}$$

Rare earth doped crystals

For the case of cerium doped YSO treated in this thesis there are several phonon-levels which the ion can decay to. But all these levels decay to the lowest ground state very quickly by phonon-emission. Thus, the system behaves almost like a two-level system, with the only difference of multiple decay paths, its schematic diagram is shown in figure 5b. The spontaneous decay emission coefficient, A_{21}, is changed for the sum of Einstein coefficients for all decay paths to the ground state, $\sum_{i=1}^{\infty} A_{2i} = \tau_1^{-1}$. The lifetime, τ_1, is defined as the time after which only a little fraction of atoms has not yet decayed. With this the equation (2) can be rewritten as:

$$N_1 - N_2 = \frac{N}{1 + 2I(\omega)\sigma(\omega)/(\hbar\omega \sum_{i=1}^{\infty} A_{2i})} = \frac{N}{1 + I/I_s(\omega)}. \tag{5}$$

The minimal value of $I_s(\omega)$ occurs at the peak of the homogeneous line shape function, $g_h(\omega)$, where the absorption cross-section is the largest, i.e. $\sigma(\omega_0) = \sigma_0 g_h(\omega_0)$, and is denoted as $I_{sat}=I_s(\omega_0)$, this expression is precisely what one refers to when talking about the saturation intensity. Where σ_0 is the integrated absorption cross-section, and g_h is defined to that $\int g_h(\omega)d\omega = 1$ Taking equation (3) and using the lifetime defined above it can be rewritten as:

$$I_{sat} = \frac{\hbar\omega}{2\tau_1\sigma_0 g_h(\omega_0)}. \tag{6}$$

At the resonance frequency ω_0 the lineshape function is $g_h(\omega_0) = 8\tau_1\tau_2\pi^{-1}$, where τ_2 is the *coherence time*, i.e. a quantum mechanical effect describing the time that a system can stay in superposition of two states. At this point the saturation intensity can be directly related to the homogeneous linewidth of a transition, $\Gamma_h = \pi^{-1}\tau_2^{-1}$, and it is expressed as:

$$I_{sat} = \frac{\pi\hbar\omega}{16\sigma_0\tau_1^2\tau_2} = \frac{\pi^2\hbar\omega\Gamma_h}{16\sigma_0\tau_1^2}. \tag{7}$$

σ_0 can be easily calculated from the known absorption, α_0, and the known number of ions in the laser focus, N, as $\sigma_0 = \alpha_0 N^{-1}$. The life time, τ_1 is know for Ce:YSO & Pr:YSO that is 40ns and 164μs respectively. While this model is

assumed for CE the Pr:YSO can seen as a two level system at low temperatures, down to the points where slightingly above 4K its hyperifne levels gets so sharp that that optical pumping begins and it can no longer be regarded as a two level system.

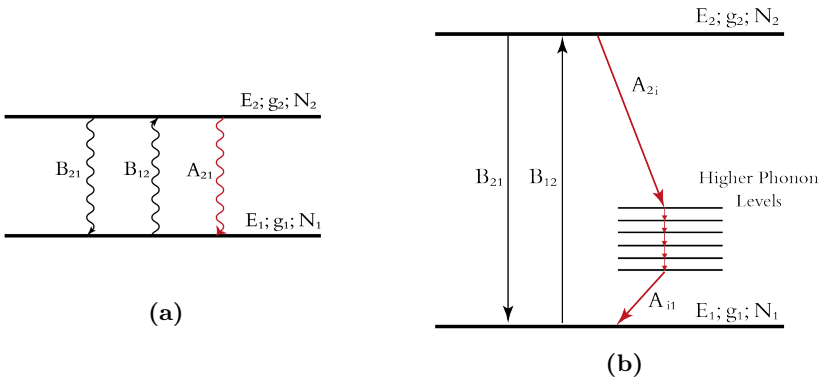

Figure 5: (a) An idealised two level representation of an atom. Both levels are energy degenerate, g_1 and g_2. Einstein's coefficients are intrinsic properties of an atom that describe its interaction with intense laser light: spontaneous emission, A_{21}, absorption coefficient, B_{12}, and stimulated emission, B_{21}.
(b) The 5d-4f transition in Ce:YSO can be appxoximated as a two-level system, since there are several phonon-levels which the ion can decay to that are only very short lived intermediate states. The spontaneous decay emission coefficient, A_{21}, is changed for the sum of Einstein coefficients for all decay paths to the ground state, $\sum_{i=1}^{\infty} A_{2i} = \tau_1^{-1}$. All other variables are the same as in (a).

Power Broadening

For an ion transition in a crystal saturation effects become particularly important due to the presence of the inhomogeneous absorption profile. In response to the increase of laser field intensity the central transition get saturated and the atoms in the wings of homogeneous broadening whose transitions overlap with the laser frequency start to get excited instead (figure 6 gives a schematic representation of this process). The reason for this is *power broadening* — the effect describing the increase in the absorption coefficient line width with intensity.

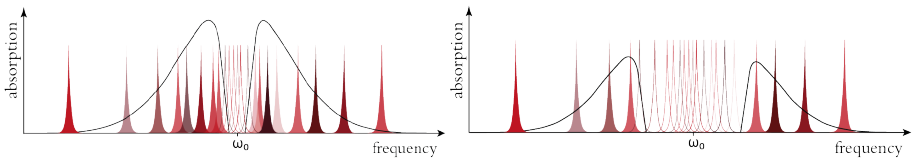

Figure 6: In a crystal saturation effects become particularly important due to the presence of the inhomogeneous absorption profile. The schematic plots represent as in response to the increase of laser power (from left to right) central transitions get saturated and the atoms in the wings of homogeneous broadening whose transitions overlap with the laser frequency start to get excited instead.

The power broadening contribution is contained within the absorption coefficient in equation expression (1) and it is expressed by Foot [9] as:

$$\kappa(\omega, I) = N\sigma_0 \frac{\Gamma_h^2/4}{(\omega - \omega_0)^2 + (\Gamma_h^2/4)(1 + I/I_{sat})}, \tag{8}$$

the absorption coefficient has a Lorentzian line shape with its peak at ω_0.

2.4 Simulation

In this section the key equations used in the simulation are introduced.

The expression that gives the number of photons emitted by the excited population of ions sitting inside a crystal is obtained by rearranging the equation (2). Knowing that N=N_1+N_2 and for convenience referring to the upper energy level as the excited level, $N_2 \equiv N_{exc}$, we get:

$$N_{exc} = \frac{N(\omega)}{2}\left(1 - \frac{1}{1 + I/I_{sat}}\right). \tag{9}$$

The homogeneous broadening of ions sitting in a crystal results in variation of saturation intensity over frequency. One can arrive at the desired mathematical expression for equation 9 that includes the latter by substituting the eq.(8) into eq.(1) and rearranging ($\kappa(\omega)$ is replaced with eq. 8 accordingly) :

$$N_{exc} = \frac{N(w)}{2}\left(1 - \frac{1}{1 + (I/I_{sat})\frac{\Gamma_h^2/4}{(w-w_0)^2+\Gamma_h^2/4}}\right).$$

As a result of lattice strains the population of Ce ions in the crystals spread out in a Gaussian distribution (inhomogeneous broadening) as a function of transition frequency:

$$N(w) = \frac{N_0}{\sqrt{2\pi}} \frac{\sqrt{8ln2}}{\Gamma_{in}} \exp\left(-\frac{(w - w_0)^2}{2(\Gamma_{in}/\sqrt{8ln2})^2}\right)$$

Putting everything together we get:

$$N_{exc} = \frac{\frac{N}{\sqrt{2\pi}} \frac{\sqrt{8ln2}}{\Gamma_{in}} \exp\left(-\frac{(w-w_0)^2}{2(\Gamma_{in}/\sqrt{8ln2})^2}\right)}{2}\left(1 - \frac{1}{1 + (I/I_{sat})\frac{\Gamma_h^2/4}{(w-w_0)^2+\Gamma_h^2/4}}\right). \tag{10}$$

Finally, approximating the laser beam sent through the crystal to be a Gaussian beam the expression for intensity is taken from Saleh and Teich [12]:

$$I(\rho, z) = \frac{2P}{\pi W^2(z)} \exp\left[-\frac{2\rho^2}{W^2(z)}\right], \tag{11}$$

where P stands for the beam power, ρ is the radial coordinate and the beam radius is given by $W(z) = W_0\sqrt{1 + \left(\frac{z}{z_0}\right)^2}$, where $z_0 = \pi W_0^2/\lambda$ is the Raleigh length and W_0 is the beam waist.

3 Method: Simulation

The code simulates the number of photons that are collected by the fluorescence detection setup (see section 4.2.2) from the excitation volume of RE doped bulk crystal as the function of the power of the excitation laser. The simulation assumes an idealised two-level system for the relevant transitions and includes the effects of power broadening.

The initial version of the code describing the characteristics of the setup and excited medium was written by Karlsson [13], the supervisor of the project. The technical parameters of the optical components used in the setup such as focal length of lenses and the size of a pinhole (see section 4.2.2) were included into the code. The collection efficiency of the setup entered the code as a constant that was previously calculated by Karlsson [13]. Likewise, the properties of the excitation ions such as their life time and doping concentration are the parameters of the code, allowing to use the code for both Pr and Ce simulation. The code was developed further to include the power broadening effects and get the saturation intensity curves.

At the beginning of writing the script a number of problems were faced that prevented us from running the simulation. As the power broadening included the frequency variable, the initial difficulty was caused by a 4D integral that no Matlab function could handle directly. A number of combinations including that of a 3D integration *triplequad(x,y,z)* function and 'for loop' were tested but none gave a satisfactory result — simulations running several hours or even days but giving very poor accuracy was the best one could expect. First results followed after employing the 'for loop' to perform the whole integration. In general this is a very slow integration method, but it was used as a starting point; a better approach would have been using matrices in the same way. However, after reviewing the formulas it was decided to optimize the code taking into account the cylindrical symmetry of the problem, i.e. using the coordinate transformation the 4D integral was reduced to a 3D case. After this change the previously attempted *triplequad(z,ρ,ω)* (for cylindrical coordinates instead) function was utilised again. Comparing the derived results to a rough analytic solution it was clear that after the coordinate transformation the *triplequad* solutions were better fit to its analytic counterpart than the ones from a simple 'for loop' integration.

After the simulation was working properly the code was further optimised. The next step was to set the integration limits for both spatial and frequency contribution to find optimum values that would give sufficiently accurate results, spatial optimisation process can be seen in figure 7. From the figure one can see that spectral power broadening makes the curve almost linear as compared to the ones excluding the saturation effect. This makes it more difficult to measure the saturation intensity. The final version of the code can be seen in the appendix at the end.

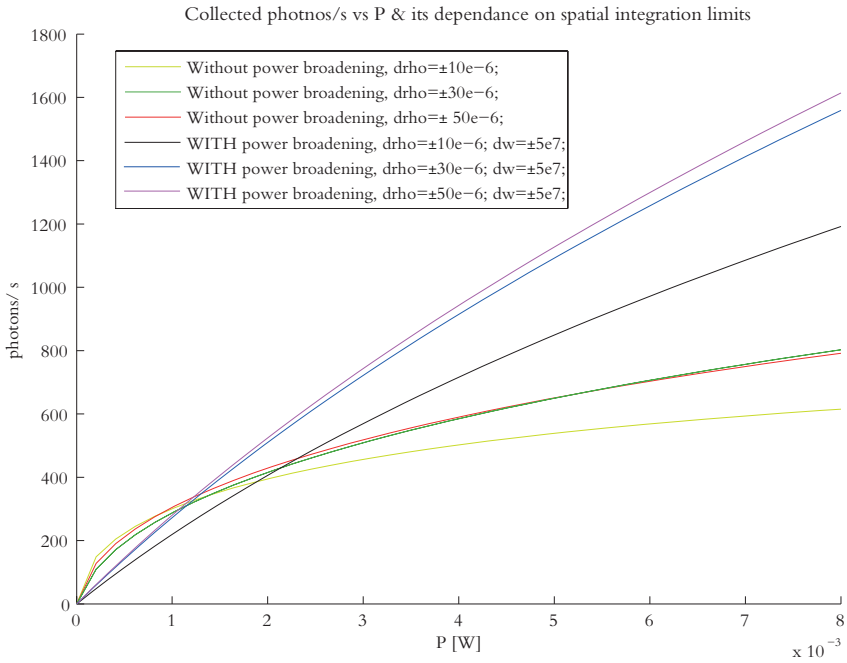

Figure 7: The plot showing the optimisation of the simulation for cerium ($I_{sat} = 10^6$ W/m^2) with both the included and excluded power broadening effect. drho stands for the integration limits of the radial coordinate, and dw denotes frequency integration limits. By examining how different spatial integration limits contribute to the result the optimum integration values were selected.

3.1 Data fitting

The script used for fitting the theoretical curves with measured data was written by Nilsson [14] during the last days of the project to aid measured data analysis. The code takes the measured data and scales the relevant theoretical curves with an optimised scaling factor. The factor, k, is calculated using the score function that is defined as:

$$score = \sum_i \frac{(e_i - t_i \cdot k)^2}{\sqrt{\sigma_{x,i}^2 \cdot \sigma_{y,i}^2}}, \tag{12}$$

where e_i is the measured data point and t_i is its closest theoretical counterpart. σ_y is the standard deviation of the measured point in y axis and σ'_x and is an expression that mimics the standard deviation in x axis by taking the limits introduced by deviation in x axis and seizing the difference in y axis between the corresponding theoretical points. During the fitting procedure the code picks the scaling factor that minimise the score.

4 Method: Experiments

Having completed the simulation the next step was to carry out an experiment that could verify the simulation results.

The base of the setup used for the experiment was developed in the master thesis by Bladh[15] that was aimed at a single ion detection setup. However, due to the lack of time in his project the work on the last bits of the setup had to enter this thesis. It was namely the work on the crystal and focusing lens holder along with the installation of a thermal link that had to be continued in this project. The thermal link was designed to maintain the heat conduction between different parts of the holder necessary for an efficient cooling of the experimental sample.

After finalising the holder the next step was to test the diode laser and align the optical setup. However, the diode laser has failed to operate and hence had to be changed for an alternative laser with a different wavelength. The aims of the thesis had to be modified accordingly. A part of this section is hence dedicated to the details of the setup and the changes that had to be made during the course of the project, along with specifications of relevant equipment as well as the principle of the measurement. The course of measurement and data processing is discussed at the end.

4.1 The Holder Design

The holder was designed to sit inside the liquid helium continuous flow optical cryostat (Optistat CFV, Oxford Instruments) hosting both a crystal and the scanning system. As experiments to be carried out using the holder require temperatures below 4K, efficient heat distribution had to be guaranteed. The resulting problem initially tackled by Bladh[15] and continued in this project was to design a thermal bridge between the cryostat cold-finger and the crystal holder (please note that in this text the whole assembly is referred to as the *holder*, while the *crystal holder* is the part that hosts a crystal sample, please see figure 8 for clarification).

The thermal bridge was supposed to connect the sample to the cryostat cold-finger and at the same time not obstruct the movement of the scanning system. The scanning system consists of three nanopositioners (2×ANPx51 and 1×ANPZ51, Attocube) and a focusing lens (f=1.2mm) taken from a blue-ray player that works both as a focusing lens for the excitation laser and as a collection lens for the fluorescence. It was crucial to have the lens inside the cryostat for a few reasons: (i) it had to be close to the sample to get a large collection angle for fluorescence; (ii) having the lens outside the cryostat, the beam would go through the cryo-window at an angle which would create aberrations and limit the laser focus. One can now see why designing a flexible and thermally efficient link was the crucial part of the holder design.

As the link as well as the thermal bridge were manufactured from from oxygen annealed copper, it had to be very thin to make scanning possible. The evolution of the holder from the blueprint to the actual assembly including detailed specifications of the holder parts can be seen in figure 8; one can also see where the link was supposed to be installed. The optimisation of this design was continued in this project.

Initial experiments carried out within the framework of this thesis examined the heat conduction via the thermal bridge of the holder. For the first cooling experiment the thermal link was simply clamped into the dedicated cavities (see point (9) in figure 8) and the holder was attached to the cryostat cold-finger that was cooled to the cryogenic temperatures. During the experiment the change in temperature of both the cryostat cold-finger and the crystal holder were measured simultaneously (the location of the temperature sensors is indicated by point (s) in figure 8). The result of the experiment showed unsatisfactory outcome as the cooling procedure took around 7 hours before the experiment was terminated, and the temperature had not fallen below the desired 4K threshold (see figure 13 in section 4.1.3). In order to understand the thermal behavior of the copper link and explain the reason behind the failure the *residual resistance ratio* (RRR) measurement was carried out next.

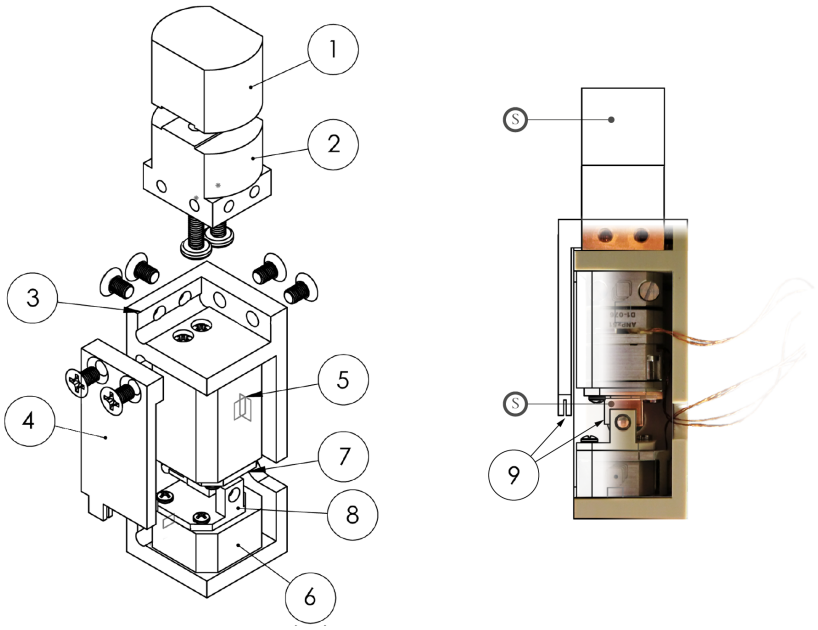

Figure 8: The holder design evolution up to the point from where it was continued in this thesis. *LHS*: a schematic drawing of the holder parts[15] (note the arbitrary scale): (1) cryostat cold-finger (part of the existing cryostat, copper); (2) finger adapter (copper); (3) holder (main supporting structure, PEEK); (4) cold bridge (copper); (5) two nanopositioners for sample scanning; (6) nanopositioner for lens focusing; (7) crystal holder (copper); (8) blue-ray lens holder (PEEK).
RHS: The actual holder as manufactured from the blueprint; three attocubes and the blue-ray lens can be seen mounted. The design has been optimised from here onwards. (9) The cavities for attaching a flexible copper link; (S) the points where the temperature sensors (DT-670-SD-1.4L, Lakeshore) were attached in order to measure the temperature difference between the cryostat-finger and the crystal holder.

4.1.1 Residual Resistance Ratio

It is hard to specify the thermal properties of a sample at cryogenic temperatures because depending on the purity and treatment its thermal conductivity varies over many orders of magnitude. It is therefore necessary to perform a measurement on a sample in each case. This section is dedicated to introducing an index for evaluation of the thermal performance of a sample and its utilisation on testing the copper link.
The direct thermal conductivity measurement on a sample is very difficult, but it can instead be determined relatively easily from the electrical resistivity measurement through the Wiedemann-Franz law [16]. The electrical resistivity can be approximated to be constant over a range of very low non-superconducting temperatures and is refered to as *residual resistivity*. It is in turn used to calculate the residual resistivity ratio, RRR, that is defined as the ratio of the resistivity at the room temperature of a material and its residual resistivity:

$$RRR = \frac{\rho_{@20^{o}C}}{\rho_{@cryo.T}}. \tag{13}$$

It serves as a general index of the purity and the thermal performance of a sample; a high index implies high conductivity at the cryogenic temperatures and *vice versa*.

As for the reference we looked at the article by Woodcraft [16] that mentions that the RRR index of a copper sample can be as low as 5 and rise to over 2000 after an oxygen annealing process. For this reason the copper link used in this project was manufactured from the purest (5N purity) copper and then treated in an oxygen annealing process expecting a high RRR index.

The RRR experiment

The RRR experiment was carried out by simultaneously performing a voltage and current measurement on a copper link while cooling it down to 3K temperature. Due to a high anticipated RRR a high current source was needed to measure low resistance.

As it is seen in figure 9 the link was soldered to two thick copper wires supplying high current from a high current generator (Lakeshore 625) and two thin wires soldered to the link slightly closer to the center in order to measure the voltage. The copper link dimensions in between the latter two points were carefully measured in order to calculate the resistivity using the well know formula: $\rho = R\frac{A}{l}$, where A is the cross-section area and l is the length of the link, and R is the resistance that was deduced from the measured data using the Ohm's law. The measurement outcome can be seen in figure 10 below. The corresponding RRR values from both measurements gave the mean value of 167.5, which is much lower than expected.

The poor result can be explained by the poor quality of the sample and the failure of the annealing process. As one is informed by Woodcraft [16] "large reduction in conductivity is caused by even a few ppm (parts per million) of magnetic impurities in copper $\langle \cdots \rangle$ the 5N specification only describes the total impurity content and not the quantity of individual elements", hence different samples from the same ore can have completely different RRR. It is hence hard to say whether it was the oxygen annealing process that has failed, whether

it was poor quality of the sample, or both. As the plan did not work out silver soldering the copper link to the crystal holder and the cold bridge was re-considered, which was set aside in the first place as it is well known that high temperatures destroys the result of the carefully temperature controlled annealing process.

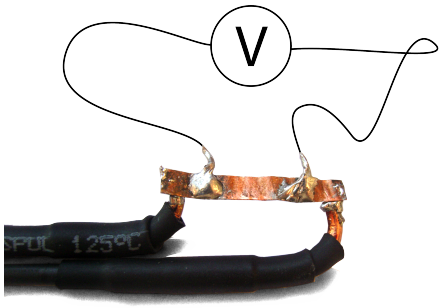

Figure 9: A copper link after the RRR measurement. Thick copper wires were supplying the current, a voltmeter was connected to the other two soldering points.

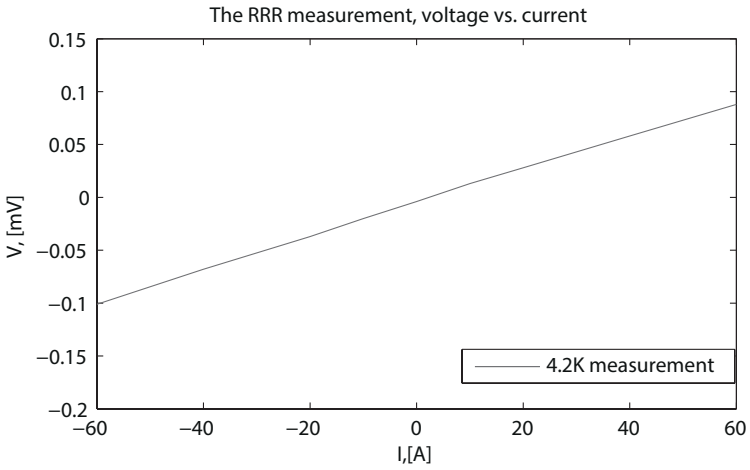

Figure 10: The plots show the voltage dependence on the driving current flowing through the investigated oxygen annealed copper sample at cryogenic temperatures.

4.1.2 Improvements to the design

As suggested in the thesis by Bladh[15] the further step was gold-plating all the copper parts making the holder less susceptible to the absorption of heat radiation and protecting the copper surface from oxidation which could worsen the heat conductivity at low temperatures. Some parts before and after gold-plating can be seen in the figure 11. As no experiments were carried out before the plating, there is no way to see the overall improvement. However, as this has reduced the absorbed heat the thermal requirements for the link were lowered correspondingly.

For the next step the flexible thermal link was installed into the holder by silver soldering and getting ready for the final cooling experiment.As it can be seen from the figure 12a silver soldering procedure required heating of the copper parts which destroyed the improvements gained during the annealing process. The resultant performance of the improved holder (figure 12b) in the cooling experiment is discussed below.

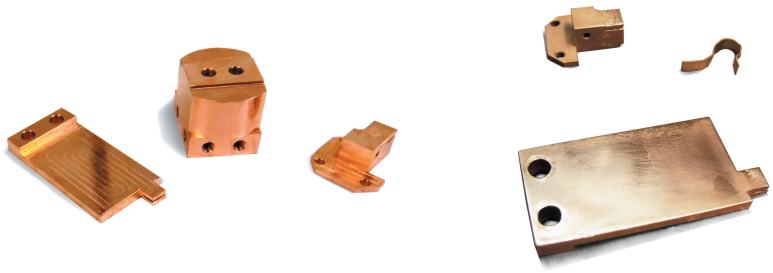

(a) **(b)**

Figure 11: (a) The holder oxygen-annealed copper parts before gold-plating. (b) Some parts including the link after gold-plating.

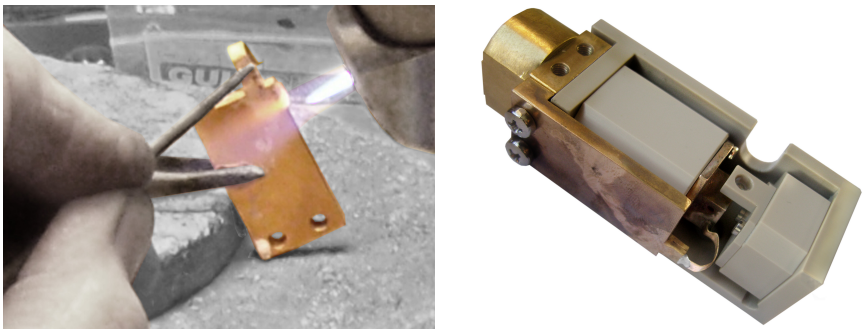

(a) **(b)**

Figure 12: (a) The process of silver soldering. (b) The mounted holder with gold-plated and silver soldered parts. Nanopositioners are here replaced with mock-cubes made of PEEK (plastic).

4.1.3 The Result of Cooling Experiments

The last cooling experiment was carried out and compared to the result obtained before the soldering procedure. A small improvement in the cooling pattern of the crystal holder has been observed after silver-soldering the gold plated copper link. As one can observe from figure 13 the cold-finger was cooled down with a higher rate in the last experiment, hence it is hard to say whether the temperature of the crystal holder follows that of the cold-finger closer than in the first case. The important point however is that in the last experiment the sample holder cools down below 4K, which was not achieved without the soldering and gold plating of the link. It does however take hours for the sample holder to cool down as compared with mere minutes of the cryostat finger case.

In both cases around the temperature of 35K a phenomenon is observed that dramatically slows down the process of heat conduction. It can be attributed to the change in heat conduction mechanism: above 35K the conduction is mediated by phonons, below this temperature heat is transported by electron movement.

To sum up, seven hours cooling time is not acceptable in the long run and it might be better to use the available helium bath cryostat that exposes the holder directly to helium instead of transferring heat via copper thermal bridges. The cold-finger cryostat was however preferred for its compact size and good access to the sample that makes the aligning procedure easier, and that is why the holder was designed in such a way.

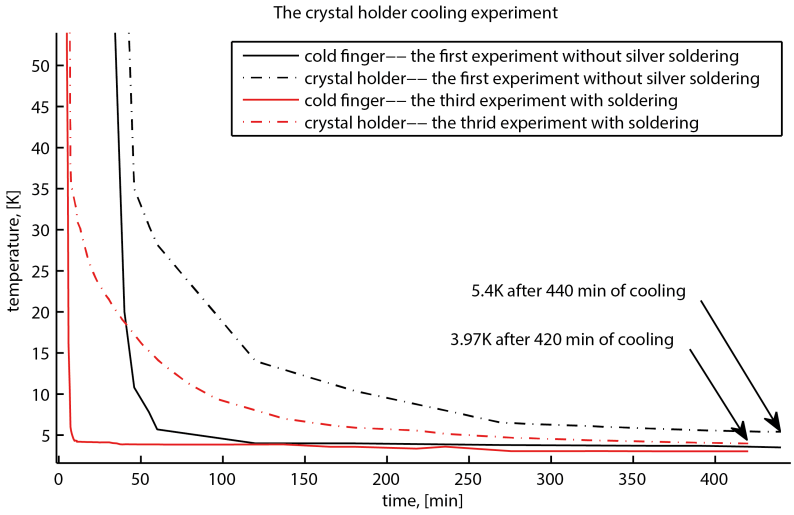

Figure 13: In both crystal holder cooling experiments an abrupt slow down in the exponential cooling pattern can be observed around 35K. Due to different cooling rates it is hard to see the difference in cooling patterns. However, in the first case the crystal holder is not cooled below 4K, while in the second the temperature of 3.97K is reached.

4.2 The Saturation Intensity Measurement Setup

At this stage of the project the simulation of the experiment and the holder were complete – the next step was to conduct the experiment itself. However, some of the equipment has failed therefore the objectives of the project along with the experimental setup had to be slightly modified.

The initial goal of the project was to measure the saturation intensity of Ce ions in an yttrium silicate crystal environment. Unfortunately, one of the 370.7 nm diode lasers was destroyed by electric discharge in another experiment. The spare one turned out to be too old and could not be tuned to 370.7 nm. A new laser was not acquired within the time span for this thesis either. Therefore, the objective of measuring the saturation intensity of Ce was postponed until a new laser arrives. An equivalent experiment only on Pr that allowed to test the validity of the simulation was carried out instead.

Finally, the experimental setup for exciting Pr^{+3} ions within an yttrium silicate crystal host environment was prepared and the experiment was carried out. The schematic figure of the experimental setup is depicted in figure 14. The whole setup can be divided into three parts: (i) the cooling cryostat with a sample, (ii) an excitation laser system, (iii) a fluorescence collection setup along with data recording equipment. The cryostat was briefly addressed in section 4.1, other two parts along with specifications of relevant equipment are addressed separately below. The section is ended reviewing the course of measurement and data processing.

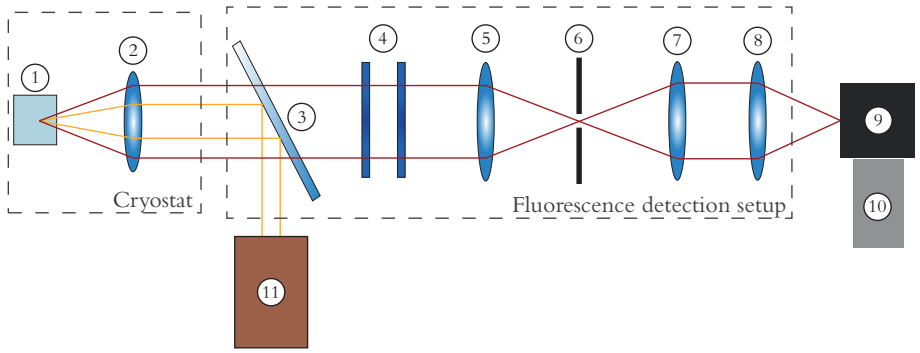

Figure 14: *Setup scheme*: (1) crystal; (2) blue-ray lens; (3) 70:30 beam splitter; (4) two emission filters; (5) focusing lens; (6) pinhole; (7) collimation lens; (8) focusing lens; (9) spectrometer; (10) camera; (11) excitation laser system.
Changes to the initial setup: due to the 370.7 nm laser (11) failure a Pr^{+3} doped crystal (1) was used instead of a Ce crystal; a 606 nm excitation laser system (11) and different fluorescence band pass filters (4) were used accordingly.

4.2.1 Excitation laser system

Before telling whether the spare external cavity diode laser could replace the destroyed diode it had to be tested. The spare diode had been used for a long time and was showing the apparent signs of decay: the power of the diode laser was as low as 1.5 mW as compared to 8mW of a new diode of the same kind.

At first the external cavity diode laser was aligned into the the Michelson interferometer of the wavemeter that was manufactured as a part of the master project written by Hertz and Nilsson [17] back in 80's. Since the wave meter was out of use for some time it had to be re-aligned. The alignment procedure was aided by the guidelines given in the thesis itself [17]. As after a number of trials the laser could not be tuned to the desired wavelength it was decided to test its spacial and frequency mode structure. The spatial beam profile of the laser diode turned out to be extremely bad with very little similarity to the preferred TM_{00} mode (see figure 15a). By aligning the laser beam into a scanning Fabry–Pérot interferometer (SA200-3B, Thorlabs) with a 1.5 GHz free spectral range the spectral mode structure could be observed while tuning the wavelength. The aim was to tune the external diode laser cavity to the single frequency mode regime. After numerous attempts the laser could not be tuned to the desired 370.7 nm wavelength (see figure 15b). It was concluded that the laser was too weak to work in a single mode and to be tuned to the desired wavelength.

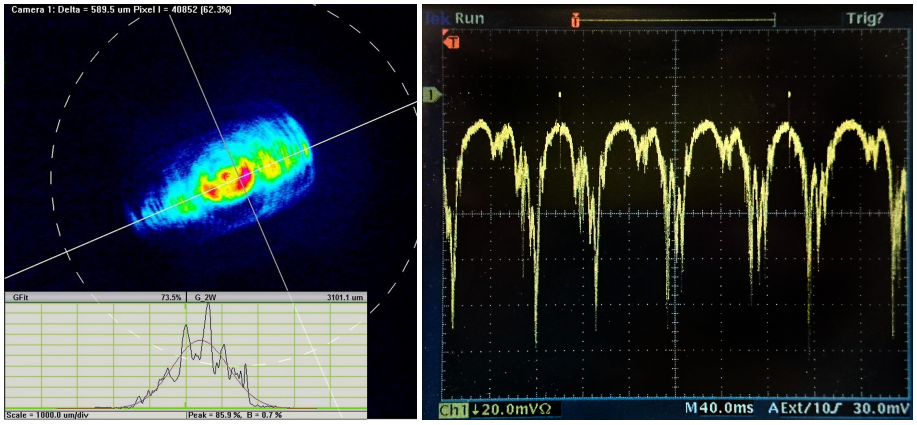

(a) **(b)**

Figure 15: (a) The spatial mode of the external cavity diode laser. Blue laser diodes always have a bad spatial profile, but the observed profile is even worse than normal. It is impossible to tell whether the profile is a sum of a few modes or infinitely many, it may even be cause by some dirt on a diode. (b) Frequency mode of the laser is clearly showing the multimode lasing.

606 nm ring cavity dye laser

A commercial dye laser (CR-699 Ring Laser, Coherent) was employed for the excitation of Pr^{+3} ions replacing the failed diode laser system. The laser is continuously pumped with Rhodamine 6G dye that in turn is optically pumped by a higher energy pump laser (Millenia Pro, Spectra Physics).

Regardless of the deviation from the initial goal of the project, the dye laser system offered many advantages for the execution of the experiment. Considering mere testing of the validity of the simulation the immediate advantage of the dye laser followed from its high power output that can be optimised up to 1 W. Moreover, the setup alignment procedure was strongly facilitated by

high power output. The laser is scannable in a wide range of wavelengths and has a linewidth of about 1 MHz. This made it easy to tune it to the 605.977 nm wavelength needed for the Praseodymium $^3H_4 \rightarrow {}^1D_2$ transition excitation. However, before starting the alignment of the setup the laser had to be stabilised and coupled into an optical fiber (P3-488PM-FC-5, Thorlabs).

In the beginning of the experiment preparation the ring cavity laser would fail to start and had to be optimised every following day. It was decided to realign the laser from scratch. The alignment was aided by the laser manual. After aligning the ring cavity and adjusting the dye jet and having inserted all the components the laser had 400 mW power output. The time spent on stabilisation proved to be worth the effort as the laser system was running smoothly for the rest of the project.

4.2.2 Fluorescence Detection setup

Modifications had to made to the initial design by Bladh [15] to accommodate Pr fluorescence detection. The actual fluorescence detection setup can be seen in figure 16. First of all, the mirrors were changed to reflect in the desired wavelength region (BB1-E02, Thorlabs); the beam splitter and emission filters were changed accordingly. Finally, due to high excitation laser power, a spectrometer with a *charge-coupled device* (CCD) camera were used instead of the previous camera. The specifications of the key components used in the setup are given below.

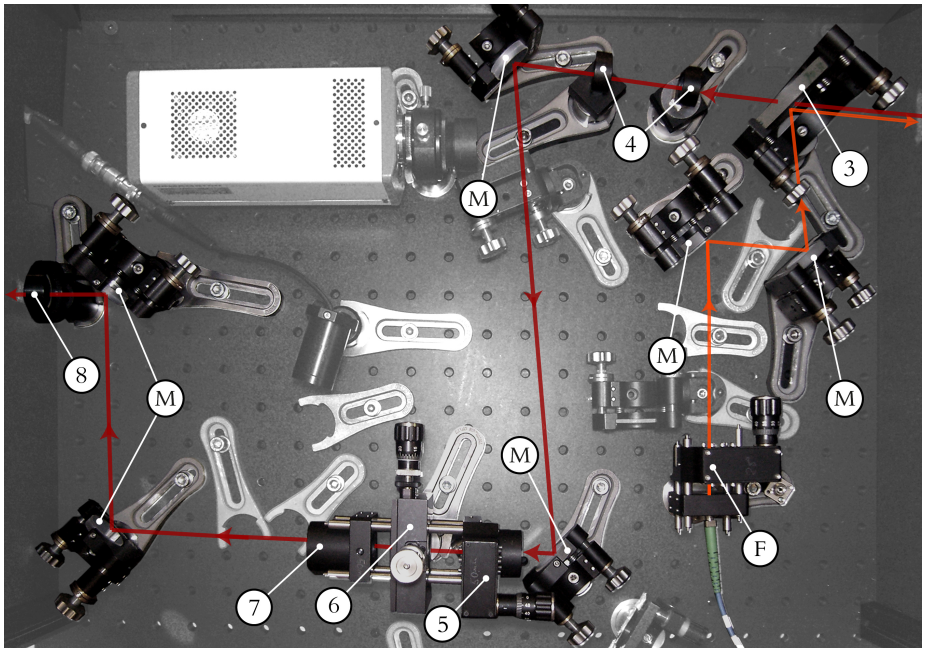

Figure 16: The components used for Pr fluorescence detection are marked out in a different color to separate from unused components from the initial Ce fluorescence detection setup. The same enumeration of the relevant components as in figure 14 is kept for consistency; secondary components are marked by a letter. The orange line denotes the excitation laser beam, while the red stands for the path of the collected fluorescence. The relevant setup components are as follows: (3) beam splitter; (4) emission filters (HQ610LP); (5) focusing lens; (6) 25 μm pinhole; (7) collimation lens; (8) focusing lens; (M) mirrors (BB1-E02); (F) fiber coupled 606 nm dye laser output.

Pinhole/Confocal microscope

The role of the pinhole in the setup is to act as a spatial filter for the emitted fluorescence. In this way the fluorescence detection setup is in fact a confocal microscope. Normally, this is not used in saturation measurements. We however wanted to exclude spacial effects and so reduce the measurement volume. Since the laser is focused onto small region within a crystal we wanted to measure the saturation effects in this small region only, but not from the regions that spreads through the whole depth of the the crystal where the beam is out of

focus. With increasing power Pr^{+3} ions in the surrounding volume starts to get saturated as well. Unless fluorescence from these surroundings is blocked by a pinhole, one will see a linear power-fluorescence signal relationship without being able to observe saturation effects at the laser focal point. As an aggregate of the confocal microscope the pinhole limits the depth of the radiation collection volume. The size of the pinhole (25μm) is selected to match the laser focus size in the crystal (considering the magnification of $\times$42).

One can see that the actual collection setup (figure 16) is assembled with respect to the confocal microscopy working principle (figure 17).

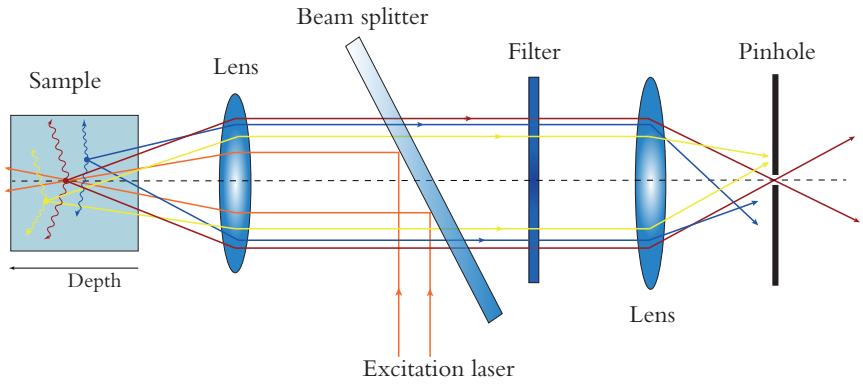

Figure 17: The confocal geometry limits the depth of the radiation collection volume. The fluorescence from out of focus points is rejected by the pinhole. The filter removes the reflected excitation laser light that passed through the beam splitter.

Emission filters

Two emission filters (HQ610LP, all Chroma Technology) were used in the setup to filter out the excitation laser spectra from the collected fluorescence. The plot showing the range of wavelengths that are passed by the filter can be seen in figure 18 below [18].

Emission filters had to be carefully aligned into the setup in order to maximize the performance. Due to the high power of the laser two filter were used.

Spectrometer and CCD detector

After passing through the detection setup the collected fluorescence is focused onto the 100μm size slit of the spectrometer (MS125 Spectrograph, Oriel Instruments). The fluorescence is detected using an intensified CCD camera with 1024 $\times$ 128 pixels resolution (DH501-25U-01, Andor Technology) [19]. The camera has several different gain-settings allowing the detection of both strong and very weak signals. The collected data is further analysed on a computer.

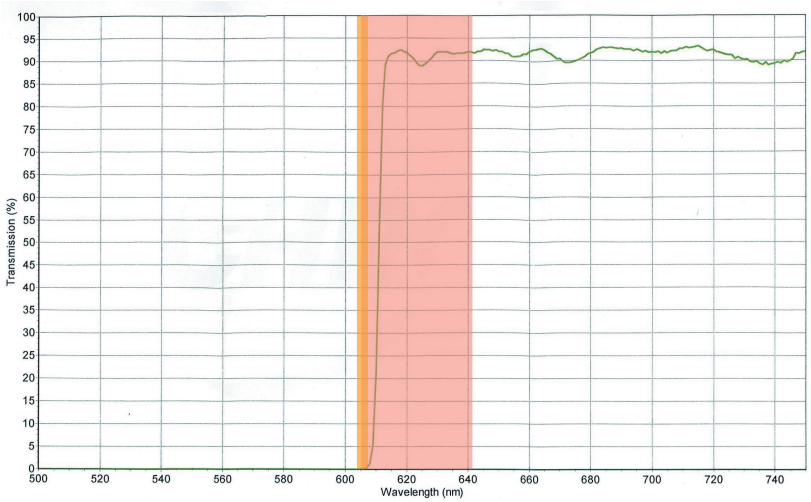

Figure 18: HQ610LP emission filter attenuates radiation with a wavelength below 610 nm, while it is approximately 94% transparent to higher wavelength radiation [18]. Approximated excitation laser range marked in orange stays outside the transmitted radiation range contrary to the mostly transmitted emission spectra marked as red.

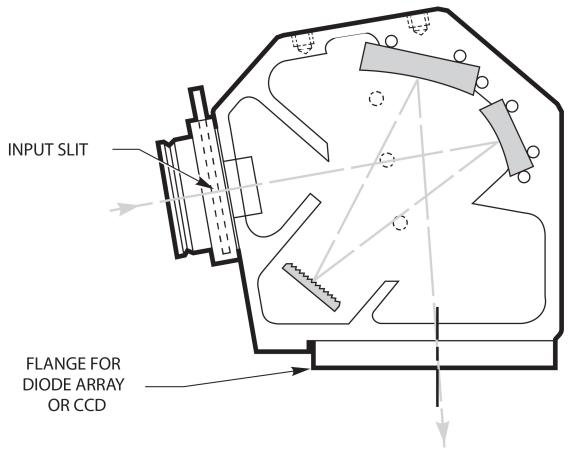

Figure 19: The optical configuration of MS125 spectrometer consists of a 100μm slit, two concave mirrors and a 1200 l/mm grating. The 100^o separation of the input and output faces along with special light blocking ribs ensure that no unwanted or reflected light reaches the the CCD detector [19].

4.2.3 The course of measurement & data processing

When all preparations for the experiment had been done measurements were carried out. Initial measurements were attempted at room temperature until a good signal was obtained, then they were followed by measurements at cryogenic temperatures.

As no signal could be observed in the beginning, it was decided to change from 1% to 0.05% Pr^{+3} ion concentration crystal. The decision stemmed from the presumption that at such high concentration energy is migrating from ion to ion in the crystal and a large part of the fluorescence is quenched [13]. This line of reasoning has proven to be fruitful as after pinhole realignment a clear signal occurred (see figure 20). The first experiment was carried out at room temperature. Then the sample was cooled down to 30K, 10K and 4.5K and respective data sets were taken.

The fluorescence spectra and its intensity were recorded by the CCD camera, while the power was measured by a power meter (FiledMaster, Coherent). As the measurements were carried out at very low powers that could not be measured directly, an attenuation factor was derived by measuring higher power before power attenuator and in front of a sample. The power on a sample was then obtained by dividing the power before the attenuator by the attenuation factor.

Windows operational system supported program Androm MCD was used to read off the CCD camera recorded spectra saving them as *SIF* multi-channel image files. The files then were further processes using a Matlab script *sifread.m* available at the official webpage of Matlab. From this point all the data was processed using ordinary Matlab commands.

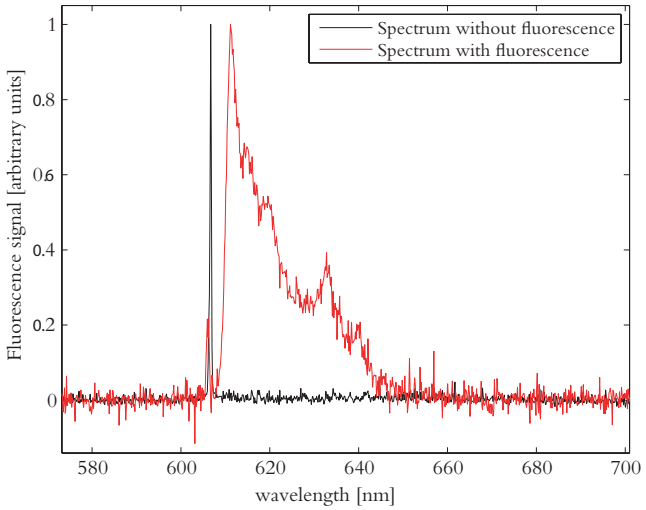

Figure 20: Attempts to measure the spectrum of Pr in a bulk crystal: first spectrum with no fluorescence but only a peak from the reflected excitation laser, the second with the fluorescence signal with the laser reflection filtered out obtained at the room temperature after the excitation crystal was changed and the pinhole realigned. Excitation laser power is arbitrary; plots are normalised to the max value of its array.

5 Results

5.1 Pr:YSO

The fluorescence spectra depicting the fluorescence originating from Pr $^3H_4 \rightarrow ^1D_2$ transition were investigated using our spectrometer (see section 4.2.2 for the technical detail). In order to obtain results that could be further interpreted the recorded spectra were integrated picking the region that excludes the excitation laser signal. This gave the quantitative expression for the fluorescence as a function of power. Finally, the fluorescence *versus* excitation power plots were fitted with corresponding theoretical curves.

To begin with, the comparison with relevant experimental data was done in order to confirm that we were observing fluorescence originating from the excitation of $^3H_4 \rightarrow ^1D_2$ transition. In figure 21a three spectra at different temperatures were recorded and as expected only weak fluorescence could be observed at room temperature in contrast to the 8K measurement where very clear peaks were seen. This is what was expected as the hyperfine levels of $^3H_4$ and $^3P_0$ that participate in the transition are so wide at room temperature that one can excite them over a wide range of frequencies, while the levels get much sharper in 8K measurement case where we can see clear fluorescence peaks instead. At 4.5K fluorescence cannot be observed anymore as at this temperature hyperfine levels become very sharp and no longer overlap.

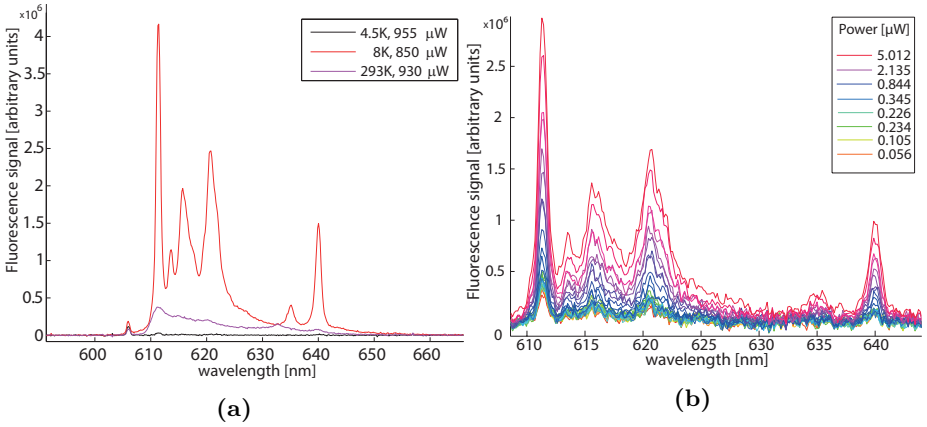

Figure 21: (a) Three spectra at comparable excitation powers but different temperatures. At 293K a weak and broad spectrum is recorded. The broad spectrum is due to a broadening of the hyperfine levels at high temperature. For the 8K measurement the transition is much narrower than for room temperature, but still wider than the hyperfine splitting. In case of 4.5K measurement the hyperfine levels become so narrow that they no longer overlap and optical pumping begins where the ions stay in long lived intermediate energy states – no fluorescence can be observed. The figure shows that 8K is a suitable temperature to perform the measurement.
(b) The fluorescence emission spectrum of Pr:YSO with 0.05% dopant concentration over a range of excitation powers at 8K temperature. The excitation laser is tuned to 605,977 nm driving the $^3H_4 \rightarrow ^1D_2$ transition. The figure illustrates that the strength of the emitted fluorescence varies with excitation power, while the shape is kept unchanged. The fluorescence emission never saturates completely but keeps increasing up to very high excitation intensities.

The spectrum recorded by Utikal et al.[11] in figure 3b shows the fluorescence originating from $^3H_4 \rightarrow ^3P_0$ excitation. Regardless of having a different excitation wavelength the spectrum is relevant as we know that after being excited to $^3P_0$ only a fraction of ions decay straight to the ground level – all other decay to the ground level through the intermediate states. For this reason the referred spectrum is similar to the one that we were aiming at measuring except the first two peaks on the right hand side. The first higher energy peak is standing for $^3P_0 \rightarrow ^3H_4$ at 488nm which is not used in our experiment. As one can see from figure 21 the second peak at the 606nm excitation wavelength was filtered out in order to get rid of reflected laser light. The spectra seen in both figures match the relevant part of the one measured by Utikal et al.[11] given in figure 3b.

Comparing three spectra recorded at similar powers but different temperatures in figure 21a very clear fluorescence signal can be observed at 8K contrary to very weak fluorescence at room temperature and no fluorescence at all at 4.5K. In case of 4.5K measurement the excited ions no longer act as a two-level system since the hyperfine structure gets so sharp that the optical pumping takes over. At the room temperature homogeneous lines get so wide that they are even wider than the inhomogeneous profile itself. In such a case the laser cannot even be tuned offline as there is absorption everywhere. As the absorption profile gets wider it also gets lower (the area under the profile is constant), thus one gets lower absorption for a specific frequency. Likewise, I_{sat} gets much higher. Hence, we have concentrated on the 8K measurement that satisfies the two-level approximation and gives clear fluorescence peaks.

Figure 21b shows that the strength of the emitted fluorescence varies with excitation power, while the shape is kept unchanged – the fluorescence emission never saturates completely but keeps increasing up to very high excitation intensities. As the 8K measurement can be approximated to be a two-level system it was studied further by integrating the fluorescence spectra and plotting it against excitation power. The data taken spreads over very wide range of excitation powers (four orders of magnitude), as it can be seen in figure 22a. Due to the high precision of the measurement most of the data points are concentrated at the low power region and therefore were shown separately in figure 22b.

Finally, the data was fitted with theoretical curves calculated with different saturation intensities, as it is seen in figures 22c and 22d. The fitting was done by running a script that scales theoretical data by a constant factor to find the best fit for the measurement (see section 3.1 for the detail). At first the scaling was done by multiplying each theoretical point by this factor. As most of the points were located in the low power region the scaling factor was optimised to fit these points, for this reason higher energy experimental points were fitted very poorly, as it is seen from figure 22c. On the contrary the data points for the lower power were fitted much better, as it was shown in figure 22d. However, due to large uncertainty in the data a single curve that fits the measurement best could not be chosen using this fitting method.

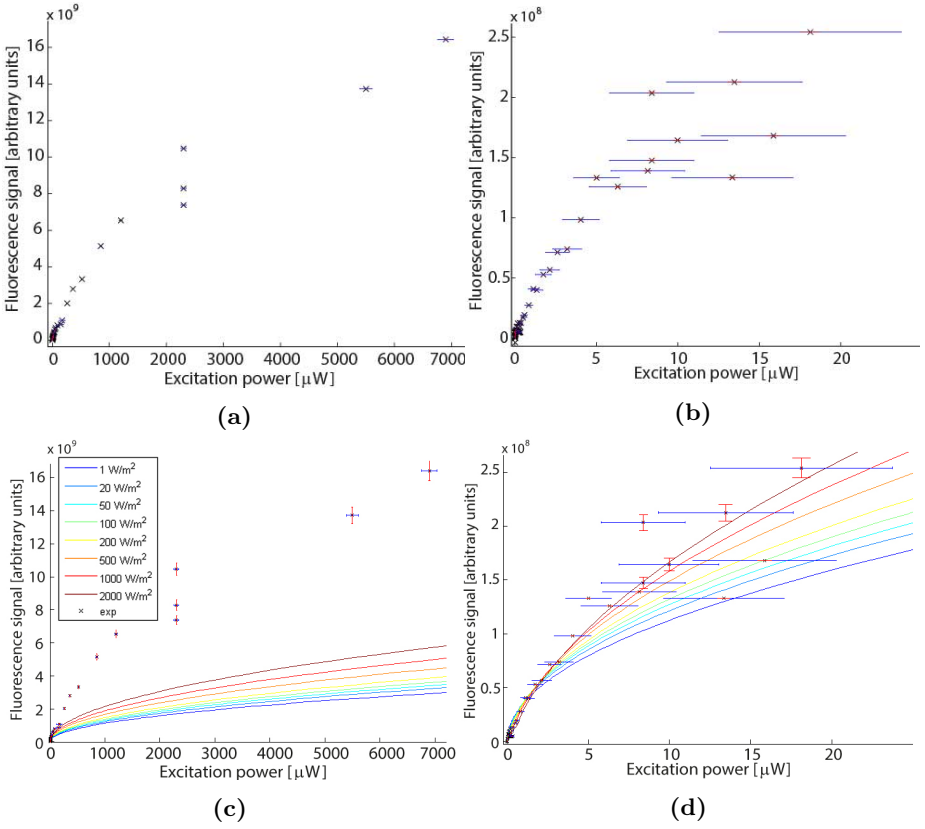

Figure 22: **(a)** The measured fluorescence as a function of excitation power ranging over four orders of magnitude obtained by integrating fluorescence spectra over a range of powers measured at 8K. The measurement uncertainty is included into the plot as error bars. **(b)** The figure is meant to show the low excitation power region that is difficult to see in fig. 22a. **(c)** The data from figure 22a fitted with theoretical curves calculated with different saturation intensities that are specified in the legend. It can be clearly seen that the fit between theoretical curves and data is very bad, especially at higher excitation powers. **(d)** The data from figure 22b fitted with theoretical curves calculated using different saturation intensities are specified in the legend of figure 22c. The plot shows the data up to an excitation power of 20 μW. Comparing to fig. 22c it can be seen that the theoretical fit is better in the lower excitation power region.

6 Discussion

As one can see from figures 22c and 22d large measurement error makes it hard to say which saturation intensity curve fits the data best. The measurement uncertainty is included into data plots in terms of error bars. The mean standard deviation of the CCD detector noise was included into fluorescence signal error. Additionally, the standard deviation was calculated on a part of spectrum without any signal but noise, this was done for each gain-setting. The power detector noise was constituted by including the power meter accuracy error and the relative error of attenuation factors (see below).

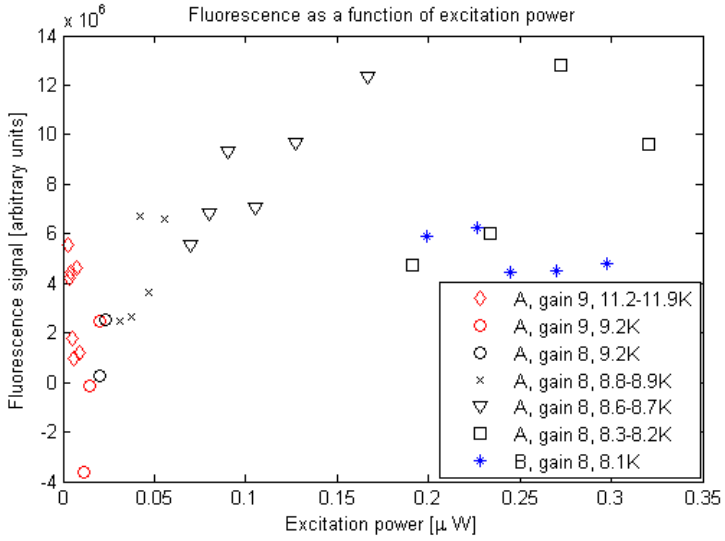

Figure 23: The figure shows the low excitation power region of 8K measurement depicted in figure 22a. Due to the limited sensitivity of the power meter the power was measured before the ND-filer introducing an attenuation factor. Capital letters A & B stand for two such power attenuation factors. Other shapes and colours presented in the legend stand for either change in temperature or gain-setting. The data subset is inconsistend due to large fluctuations in temperature.

The main error sources that have contributed to the measurement uncertainty are summarised below.

Temperature control

The linewidth of the transition is highly dependent on temperature. It can be assumed to have similar dependence as $^7F_0 \rightarrow ^5D_0$ transition of europium in Eu^{+3}:Y_2O_3 with the linewidth scaling as $\propto T^7$ [20]. In such a case even a slight temperature drift causes fluctuation of the fluorescence intensity. This explains the data discrepancy seen in figure 23 , where the discontinuity in data clearly corresponds to changes in temperature.

Attenuation factor

ND-filters were introduced in the setup to reduce the excitation laser power. For the low excitation powers due to the limited sensitivity of the power meter the power was measured before the ND-filers. Thus, the

attenuation factor of the ND-filters had to be calculated and taken into account. However, it was discovered during the experiment that such a factor was not stable. Figure 23 specify the attenuation factor, temperature and the gain-setting that was used for each data point of two data subsets of the same 8K measurement already shown in figure 22a. One can see that there is large discrepancy between the points measured before and after an attenuation factor change, where the attenuation factors are denoted as capital letters, A or B. As the attenuation by ND filters is independent of power, such behaviour was not expected. Between the power meter and the sample there was also an optical fibre. The coupling efficiency of this fibre was taken into account. However, if the coupling was not optimised, the coupling efficiency might have drifted over time; this was sadly not checked before the experiment.

Gain settings of the spectrometer

As we had to record spectra at both very low and high fluorescence signal power, different gain-settings in the spectrometer were used. Measured spectra were normalised to one gain-setting by multiplying spectra measured using other gain-settings with a factor that was defined as the ratio between the maxima of two spectra measured at the same power but different gain-setting. However, from figures 22 and 23 one can see some data points measured at the same power with different gain-setting that gave rise to different signal levels, despite compensation for the gain. As the fluorescence signal was calculated by integrating spectra, this implies that the gain of high gain-settings is not constant for different signal levels. The spectrometer uses an intensified CCD camera that multiplies the signal, very high multiplication factor of the intensified CCD camera at high gains might give rise to non-linear gain. This would explain why a fixed gain-setting is not constant for different intensities. That was not foreseen hence no intensity-sensitivity calibration was done in advance.

Laser frequency & power drift

Each time a measurement was taken the signal was being accumulated for 20 seconds. Hence it is not excluded that power and frequency of the excitation beam had shifted over that period of time.

Other error sources

In case of higher power measurement a power meter attenuator was used. During those measurements the whole assemblage had to be carefully aligned into the beam path before each measurement. It is very likely that some of the measurements were taken with a poorly optimised angle.

The data in figure 22 was fitted using the procedure described in section 3.1, which finds an optimal scaling factor for a theoretical curve taking into account each data point, its standard deviation and its theoretical counterpart. As most of the data points were concentrated at low excitation power region, the script optimised the fitting factor so that low power points with lesser uncertainty in both excitation power and fluorescence signal were fitted with best contrary to higher excitation power points.

Since the first fitting did not bear good results, after trying different approaches the curves were now scaled using a phenomenological approach, i.e.

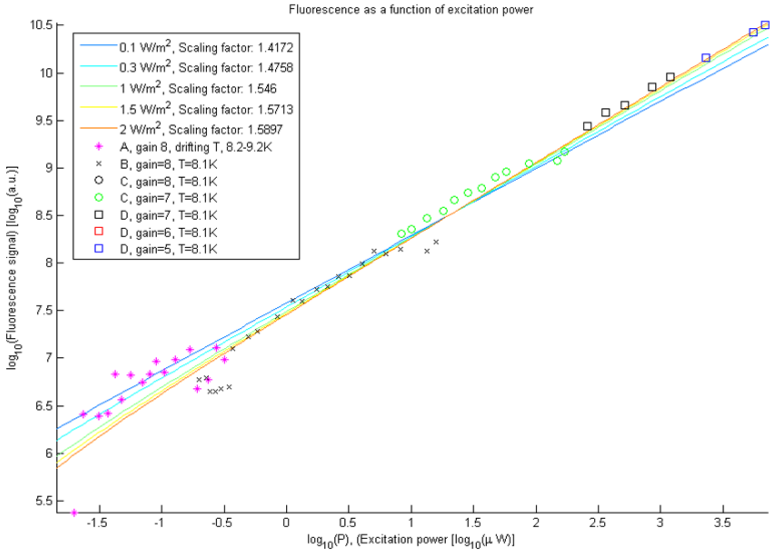

Figure 24: The measured fluorescence as a function of excitation power at 8K plotted in logarithmic scale and fitted with theoretical curves calculated using different saturation intensities that are specified in the legend. Due to instability in temperature the fitting excludes lower power points denoted in purple stars. Due to the limited sensitivity of the power meter the power was measured before the ND-filer introducing an attenuation factor, different factors are indicated in the legend as capital letters. The points measured with a different CCD camera gain-setting or different attenuation factors are marked in different colour and shape. The fit was performed using the phenomenological approach by rising theoretical points to the power of the scaling factor, scaling factors were indicated in the legend next to corresponding saturation intensities of each theoretical curve.

the same data as in figure 22a was used but it was fitted by scaling the theoretical points exponentially instead; not by multiplying, but by rising each theoretical point to the power of the scaling factor. As the data spreads out over several orders of magnitude it was later decided to use logarithmic scale instead. The outcome can be seen in figure 24. The best fit has the scaling factor of 1.5897 that does not give us any immediate conclusion on whether fitting data this way implies an error in the theoretical model used or that some of the equipment behaved in an unpredicted way scaling up the measured data.

As the scaling factor does not correspond to any immediate physical mechanism, likewise no immediate justification for the scaling method follows. No real conclusion can be reached regarding the saturation intensity. It can still be noted however, that the best fitted curves are the ones for a saturation intensity of $1\mathrm{W/m^2}$ and $2\mathrm{W/m^2}$, while the expected value for Pr is 1.8 $\mathrm{W/m^2}$. This gives us strong reason to believe that the scaling factor could be justified if only the reason for the scaling factor was found in either the theoretical code or the experimental equipment itself. On the other hand, there were too many uncontrolled error sources that contributed to discrepancies in the data. It is likely that it is measurement error that eliminated the possibility to tell which

theoretical saturation intensity curve fits the data best.

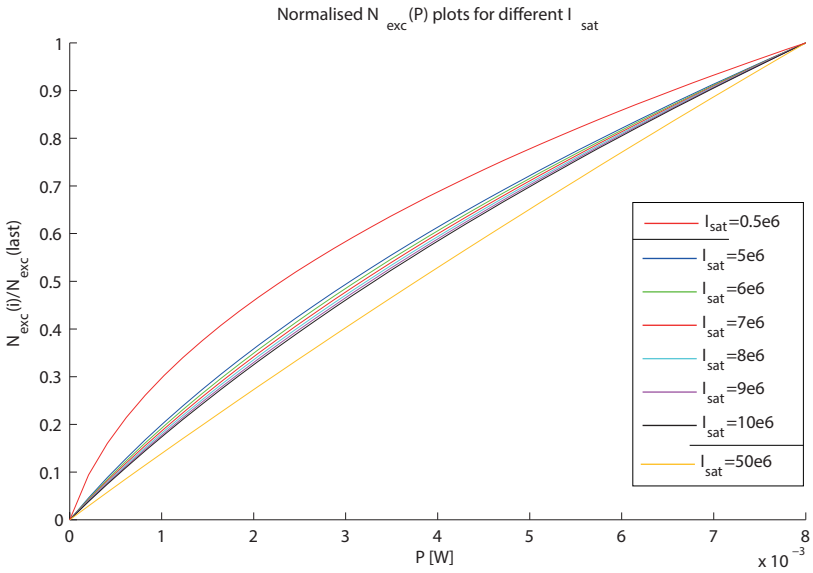

Figure 25: Theoretical Ce saturation intensity curves normalised to the highest excitation power point so that one could see the curve shape dependence on the saturation intensity. The I_{sat} [W/m^2] that is expected to be measured is in between $5{\cdot}10^6$ W/m^2 and $10{\cdot}10^6$ W/m^2, which as one can see from the figure would be very hard to differentiate.

Provided that all experimental parameters are under control such type of measurement should give I_{sat} for Ce:YSO, which was the initial purpose of this thesis. As it is well known, this measurement could not be carried out for practical reasons – only the theoretical curves are shown here instead, as that can be seen in figure 25.

Theoretical curves for Ce were normalised to the highest energy point so that we could differentiate between the shapes of curves with different saturation intensities. From the figure it is easy to differentiate between the curve shapes with $5{\cdot}10^5$W/m^2 and $5{\cdot}10^7$W/m^2 saturation intensities, it however becomes hard to tell the difference between saturation intensities that are lying in between $5{\cdot}10^6$ and $10{\cdot}10^6$ W/m^2. The measurement is expected to present a result to be found in the latter interval. Taking into account the possible error the immediate conclusion is that it would be very hard pick a single curve that fits the measurement best.

7 Conclusions

In this thesis a fluorescence detection setup, designed for samples at 4K, was finalised. The last missing part, a thin copper link to cool the sample to 4K while still allowing scanning of the sample, was installed. Finally, a crystal could be cooled below 4K using the copper link in order to carry out fluorescence detection experiments.

Fluorescence spectra of Pr:YSO were recorded at 293K, 8K and 4.5K. The fluorescence dependence on excitation power was measured with excitation powers varying over four orders of magnitude.

Data was fitted to theoretical curves. The error sources of the experiment were too severe and no conclusion could be reached regarding the saturation intensity of Pr:YSO. It is clear from the experiment that the fluorescence signal does not scale with excitation intensity as predicted by the model. The cause for this could possibly originate from both the experimental conditions, or a physical phenomenon that was not taken into account when writing the script for the model.

We can conclude that in order to measure the saturation intensity with sufficiently high accuracy one needs to gain much higher control over all the error contributing factors. One should make sure that the temperature over the duration of experiment is stable and the gain-setting of spectrometer should be calibrated accordingly. As the best fit was reached by including phenomenological scaling factor this implies that either the theoretical model used is incomplete or that some experimental equipment exhibited unexpected behaviour.

Finally, as the expected saturation intensity for Ce is much higher than that of Pr, it will be much more difficult to measure its value using the above method. Taking a look at figure 25 one can see that in the I_{sat} range of our interest the shape of normalised saturation intensity curves would be very hard to discriminate even after gaining better control over error sources.

8 Outlook

The field of quantum computing is still considered to be in its infancy and every step forward requires the uttermost effort. The work completed in this thesis is likewise just a little step towards the goal. The near future plans of the quantum information group at Lund university include the single ion detection experiment that is scheduled for the summer of 2014 as a part of the Phd project carried out by Karlsson [13]. If it was successful, I_{sat} could be measured directly on a single ion in the same way as that was already done by Utikal et al. [11].

Unless the single ion detection succeeds one should repeat the saturation intensity measurement. However, a number of lessons has to be drawn from the current project. First of all, as the homogeneous linewidth of a transition is highly dependent on temperature it has to be guaranteed that the temperature is constant for the duration of measurement. One should also make sure that the fibre coupling is optimised and the laser is frequency along with power are stabilised so that the drift during the measurement can be avoided. In case the same spectrometer and intensified CCD detector was used, one should study the gain-setting responsivity to light intensity dependence and calibrate the device accordingly. Additionally, as the fluorescence signal is calculated by integrating the spectrum and it turns out that the detector has varying responsivity depending on the incoming intensity, calculation of gain-factors by using only the maximum peak must be revised. If all the listed error sources were taken into account during the current experiment it would have been much more likely to succeed.

Finally, if neither of above experiments succeeds another alternative would be to measure the coherence time of cerium using photon echoes, but the coherence time of 4f-5d transition is so short that there is no technical possibility to carry out the experiment in the group facilities at the given time. For this reason this option was excluded in the first place.

Two further scenarios are open for the single ion detection project. In the first case, either after the first attempt or after the repeated I_{sat} measurement single ion detection succeeds and the project progresses into multiple qubit initialisation stage. In the second case, the detection experiment fails or the measured I_{sat} reveals that the homogeneous linewidth is too wide for an efficient readout, then an alternative single ion read out scheme must be developed.

The development of hardware for quantum computing is slow and the final product is not foreseen to hit the shelf any time soon. That applies equally well to rare earths based QC hardware as well as all other currently developed physical platforms. Nevertheless, the parallel with the development of the classical computer shows that even the most cumbersome idea can get shaped into excellency; or putting it into words of William Blake: “the fool who persists in his folly will become wise”.

Acknowledgements

First and foremost, I would like to express my very great appreciation to my supervisor, Jenny Karlsson, for all invaluable advise and priceless guidance through the project. Without your help this would have been a referenced fairytale at most.

I would also like to thank my co-supervisor, Professor Stefan Kröll, for his kind advice and help, and whose professional patience and reliability I deeply appreciate.

I am particularly grateful for the assistance given by my friend Kasparas Krivas, who was always keen on sharing his Matlab proficiency with me. I wish to acknowledge the help provided by Dr. Tobias Utikal, whose advice given during his visit of our group and the recently published article on a single ion detection has been a great help and inspiration for both this thesis and the single ion detection project itself. Assistance provided by Dr. Lars Rippe was greatly appreciated. I also wish to acknowledge the help provided by Yan Ying, Adam Nilsson, Diana Serrano, Andreas Walther and Qian Li.

I would like to extend my gratitude to my examiner, Mathieu Gisselbrecht, for his helpful professional advice that led to the completion of this work.

My special thanks are extended to the whole collective of atomic physics division. If I have not managed to meet you in person, I ate your cookies during Monday fika, and believe me or not – these were truly life changing cookie-eating experiences.

Last but not least, I would like to thank my colleagues Neven Ibrakovic, Piotr Rudawski, Dmitry Khoptyar, Stefanos Carlström and Chen Guo for being around.

References

[1] P.E. Ceruzzi. *Computing. A Concise History.* The MIT Press, 2012. ISBN 978-0-262-51767-6.

[2] Tom Thompson. When silicon hits its limits. *Byte*, 1996.

[3] Janus H Wesenberg, Klaus Mølmer, Lars Rippe, and Stefan Kröll. Scalable designs for quantum computing with rare-earth-ion-doped crystals. *Physical Review A*, 75(1):012304, 2007.

[4] Ying Yan. *Towards Single Ce Ion Detectin in a Bulk Crystal for the Development of a Single-Ion Qubit Readout Scheme.* PhD thesis, Lund University, 2013.

[5] Lars Rippe, Brian Julsgaard, Andreas Walther, Yan Ying, and Stefan Kröll. Experimental quantum-state tomography of a solid-state qubit. *Physical Review A*, 77(2):022307, 2008.

[6] Ying Yan, Jenny Karlsson, Lars Rippe, Andreas Walther, Diana Serrano, David Lindgren, Mats-erik Pistol, Stefan Kröll, Philippe Goldner, Lihe Zheng, et al. Measurement of linewidths and permanent electric dipole moment change of the *Ce 4f-5d* transition in Y_2SiO_5 for qubit readout scheme in rare-earth ion based quantum computing. *Physical Review B*, 87 (18):184205, 2013.

[7] Mahmood Sabooni. *Efficient Quantum Memories Based on Spectral Engineering of Rare-Earth-Ion-Doped Solids.* PhD thesis, Lund University, 2013.

[8] R Wo Equall, Yongchen Sun, R L Cone, and RM Macfarlane. Ultraslow optical dephasing in eu 3+: Y 2 sio 5. *Physical review letters*, 72(14):2179, 1994.

[9] Christopher Foot. *Atomic physics.* Oxford University Press, 2008.

[10] D Serrano, Y Yan, J Karlsson, and L Rippe. Energy transfer mechanisms in ce-pr and ce-eu codoped y2sio5 and their impact on single-ion based quantum computing. *J. Lummin.*, 151, 2014.

[11] T Utikal, E Eichhammer, L Petersen, A Renn, S Götzinger, and V Sandoghdar. Spectroscopic detection and state preparation of a single praseodymium ion in a crystal. *Nature communications*, 5, 2014.

[12] Bahaa EA Saleh and Malvin Carl Teich. *Fundamentals of Photonics Wiley Series in Pure and Applied Optics.* A John Wiley & Sons, Inc., Publication, 2007.

[13] Jenny Karlsson, 2013. personal correspondence.

[14] Adam Nilsson, 2013. personal correspondence.

[15] Tobias Bladh. Single ion detection setup. Master's thesis, Atomic Physics Division, Lund University, July 2013.

[16] Adam L Woodcraft. Recommended values for the thermal conductivity of aluminium of different purities in the cryogenic to room temperature range, and a comparison with copper. *Cryogenics*, 45(9):626–636, 2005.

[17] Hans Hertz and Lars-Åke Nilsson. Konstruktion och testning av digital våglängdsmätare. Master's thesis, Institutionen för fysik, LTH, Lund, 1980.

[18] The website of the manufacturer. `http://www.http://chroma.com/`. Accessed: 2014-04-01.

[19] Ms125 1/8m spectrograph brochure. `http://www.spectroscopic.com/Oriel/MS125_brochure.pdf`. Accessed: 2014-05-13.

[20] WR Babbitt, A Lezama, and TW Mossberg. Optical dephasing, hyperfine structure, and hyperfine relaxation associated with the 580.8-nm f 0 7-5 d 0 transition of europium in eu 3+: Y 2 o 3. *Physical Review B*, 39(4):1987, 1989.

Appendix: Simulation code

```
%with power broadening

Lx = 4e-3;
Ly = 4e-3;
Lz = 1e-3;
L = 100e-6;   %Depth of focus into the crystal

dz1 = L;
dz2 = Lz-L;
dro= 50e-6;
dw=5e7;

points=200;
P=logspace(log10(power(9)),log10((power(72)+300)),points);
P=P/(1e6);


Isat=[1 20 50 100 200 500 1000 2000 10000 15000 20000 1e5]
N_photons=zeros(length(Isat),points)


%cc = copper(8);
for j=1:length(Isat)
    j
    tic
    for i=1:length(P)

    i
N_photons(j,i)=triplequad(@(rho,z,w)...
collectedPhotons(rho,z,w,P(i), Isat(j))...
0, dro, -dz1, dz2,-dw, dw, 0.0005);

   end
  toc
%hold on
%plot(P*1e6,N_photons/N_photons(length(P)), 'Color', cc(j,:))
%plot(P/(pi*(250e-9)^2),N_photons, 'c')
%title('Collected photos/s vs. the Intensity of the incoming laser beam')
%xlabel('I [W/m^2]')
%ylabel('photons/s')
end
```

```
function N = collectedPhotons(rho,z,w,P,Isat)
%Collected photons per second from a point x,y,z in the crystal

CE_focus = 0.02;

N = CE_focus*noOfExcPr(rho,z,w,P,Isat).*CE_xyz(rho,z).*1/(164e-6);

%it is divided by the excited levels lifetime (40 ns) that tells us
%how many photons are emitted from the excited level per second,
%while CE_focus stands for all the losses connected to the optical
%system (aberration, divergence, ect.)
```

```
function CE = CE_xyz(rho,z,Isat)
%CE = CE_xyz(x,y,z)
%Collection efficiency normalized to the collection efficiency from the
%focus point

slitsize=0.025e-3; %m
%we no longer have the slit, a pinhole instead with 20 micrometers in
%diameter

f_lens = 50e-3; %m
f_obj = 1.2e-3; %m
lambda = 606e-9; %m

M = f_lens/f_obj;
slitsize_im = 1/M*slitsize;

%Assume collection efficiency follow a gaussian
W0 = slitsize_im/2;
z0 = pi*W0^2/lambda;
Wz = W0.*sqrt(1+(z./z0).^2);
CE = (W0./Wz).^2.*exp(-2*rho.^2./(Wz.^2));
```

```
function N_exc= noOfExcPr(rho,z,w,P,Isat)
%Calculates the denisty of excited Pr-ions
%at a position (x,y,z) for a given gaussian beam
lambda=606e-9;

%Doping concentrations
%concRef = 8.8e-4; %%%%%%%%we might not need it for PR
conc = 5e-4;

%Absorption coefficients
alpha =2530;
%Linewidths
gammaH = 1e3;   %Homogeneous linewidth for 4k
gammaI = 6e9;   %Inhomogeneous linewidth

%Laser parameters
% % P = 5e-6;  %Laser power at crystal surface
%we want to vary this one
W0 = 250e-9;    %Beam radius in focus
z0 = pi*W0^2/lambda;    %Rayleigh length
%Isat = 200000;  %Saturation intensity  %taken from Yan's calculation
L = 100e-6;  %Depth of focus into crystal

%Number of Ce-ions per cubic meter
Ny= 1.83e28; %No of Y per cubic meter
N = conc*Ny;

%Gaussian spread in w space
Nw=N*sqrt(4*log(2)/pi)/gammaI .* exp(-(w.^2 * 4 *log(2)/gammaI^2 ));

W = W0 * sqrt(1 + (z./z0).^2);

I=2*P./(pi * W.^2).*exp(-2*rho.^2./(W.^2)).*exp(-alpha*(L+z));

broad=(gammaH^2/4)./(w.^2+gammaH^2/4);

%times (2*pi*rho)-- Jacobian for cylindrical coordinates
N_exc = (2*pi*rho)*Nw./2.*(1-(1./(1+(I./Isat.*broad))));
```